International Journal of Radiation Oncology biology • physics

www.redjournal.org

Biology Contribution

Biophysical Modeling of In Vivo Glioma Response After Whole-Brain Radiation Therapy in a Murine Model of Brain Cancer

David A. Hormuth, II, PhD,[*] Jared A. Weis, PhD,[†,‡] Stephanie L. Barnes, PhD,[*] Michael I. Miga, PhD,[§,‖,¶] Vito Quaranta, MD,[#] and Thomas E. Yankeelov, PhD[*,,††]**

**Institute for Computational and Engineering Sciences, **Department of Biomedical Engineering, and ††Department of Internal Medicine, The University of Texas at Austin, Austin, Texas; †Department of Biomedical Engineering, Wake Forest School of Medicine, Winston-Salem, North Carolina; ‡Comprehensive Cancer Center, Wake Forest Baptist Medical Center, Winston-Salem, North Carolina; and Departments of §Biomedical Engineering, ‖Radiology and Radiological Sciences, ¶Neurological Surgery, and #Cancer Biology, Vanderbilt University, Nashville, Tennessee*

Received Jul 20, 2017, and in revised form Oct 17, 2017. Accepted for publication Dec 3, 2017.

Summary

In this experimental and computational study, 3 biophysical models are developed and evaluated for their ability to accurately describe in vivo growth and response after whole-brain radiation therapy. Models that include reduced proliferation after radiation therapy more accurately predicted future tumor growth.

Purpose: To develop and investigate a set of biophysical models based on a mechanically coupled reaction-diffusion model of the spatiotemporal evolution of tumor growth after radiation therapy.

Methods and Materials: Post–radiation therapy response is modeled using a cell death model (M_d), a reduced proliferation rate model (M_p), and cell death and reduced proliferation model (M_{dp}). To evaluate each model, rats (n = 12) with C6 gliomas were imaged with diffusion-weighted magnetic resonance imaging (MRI) and contrast-enhanced MRI at 7 time points over 2 weeks. Rats received either 20 or 40 Gy between the third and fourth imaging time point. Diffusion-weighted MRI was used to estimate tumor cell number within enhancing regions in contrast-enhanced MRI data. Each model was fit to the spatiotemporal evolution of tumor cell number from time point 1 to time point 5 to estimate model parameters. The estimated model parameters were then used to predict tumor growth at the final 2 imaging time points. The model prediction was evaluated by calculating the error in tumor volume estimates, average surface distance, and voxel-based cell number.

Reprint requests to: David A. Hormuth, II, PhD, Institute for Computational and Engineering Sciences, University of Texas at Austin, Austin, TX 78712. Tel: (512) 232-6784; E-mail: david.hormuth@utexas.edu

This work was supported through funding from the National Cancer Institute (R01CA138599, R01NS049251, R01CA186193, R21CA169387, R25CA092043, P30CA68485, U01CA174706, K25CA204599) and from the Cancer Prevention Research Institute of Texas RR160005.

Conflict of interest: none.

Supplementary material for this article can be found at www.redjournal.org.

Acknowledgments—The authors thank Drs Michael L. Freeman and Sekhar R. Konjeti for assistance and usage of the x-ray machine; Dr Erin Rericha for informative discussions; and the Texas Advanced Computing Center for providing high performance computing resources that have contributed to this research. T.E.Y. is a Cancer Prevention Research Institute of Texas Scholar of Cancer Research.

Int J Radiation Oncol Biol Phys, Vol. 100, No. 5, pp. 1270–1279, 2018
0360-3016/$ - see front matter
https://doi.org/10.1016/j.ijrobp.2017.12.004

Results: For both the rats treated with either 20 or 40 Gy, significantly lower error in tumor volume, average surface distance, and voxel-based cell number was observed for the M_{dp} and M_p models compared with the M_d model. The M_{dp} model fit, however, had significantly lower sum squared error compared with the M_p and M_d models.
Conclusions: The results of this study indicate that for both doses, the M_p and M_{dp} models result in accurate predictions of tumor growth, whereas the M_d model poorly describes response to radiation therapy.

Introduction

For glioblastoma multiforme patients, radiation therapy is typically administered after surgical resection to target any residual or inoperable cancer (1). Unfortunately, with the current standard-of-care therapy, nearly all glioblastoma patients have progressive disease 7 to 10 months after adjuvant treatment (2). Individualizing predictive models on a patient-specific basis (3) could optimize radiation therapy plans for the individual patient, to both maximize tumor cell death and minimize exposure of healthy tissue. Several groups have studied incorporating patient-specific imaging information into biophysical models of tumor growth (4-14), and recently these models have begun to include response to radiation therapy (15).

Response to radiation therapy is commonly modeled using the linear-quadratic (LQ) model, and this formalism has been incorporated into several mathematical models of radiation therapy response and planning (16-21) that use medical imaging data to initialize and constrain patient-specific tumor simulations (3). One such model, by Rockne et al (16, 17), uses magnetic resonance imaging (MRI) data acquired before and after the start of treatment to evaluate various dose schedules or estimate a patient's radiosensitivity. Corwin et al (18) expanded upon Rockne et al's model to demonstrate an approach for individualizing intensity modulated radiation therapy plans. The simulated optimized plans had a decreased exposure to normal tissue and increased time to progression, by 63% to 93% and 21% to 105%, respectively, compared with the simulated standard of care. Badoual et al (20) incorporated a model of edema in addition to radiation therapy response to recapitulate observations of post−radiation therapy growth delay. Although these patient-specific radiation therapy models demonstrate the potential value modeling has for clinical radiation therapy, the accuracy and precision of these modeling approaches need to be validated with in vivo experiments. Toward this end, in vivo imaging measurements and histologic sections are used in this study to assess the model prediction error of 3 models of response to radiation therapy.

In this contribution we systematically evaluate the ability of 3 biophysical models to describe and predict the in vivo spatio-temporal development of C6 glioma growth after radiation therapy differentiated by (*1*) cell death immediately after radiation therapy (or M_d model); (*2*) a reduction of proliferation rate after radiation therapy (or M_p model); and (*3*) the combination of cell death and reduced proliferation rate (or M_{dp} model). Diffusion-weighted MRI (DW-MRI) and contrast-enhanced MRI (CE-MRI) data acquired before and after radiation therapy are used to estimate tumor cell count. The M_d model is related to the LQ model resulting in immediate cell death; that is, after irradiation some fraction of the cells lose their clonogenic survival, eventually resulting in predominantly apoptosis or necrosis. The M_d model assumes that the effect of radiation therapy (ie, cell death) occurs over a relatively short period. The M_p model assumes that irradiation predominantly result in a reduced net proliferation of tumor cells. A dose-dependent reduction in proliferation rate has been observed in the C6 line (22) and may be due to cell cycle arrest (23) or senescence. The M_p model, however, assumes that the effect of radiation therapy is a long-term alteration of growth kinetics. The M_{dp} model incorporates the effects of both reduced proliferation and cell death to model post−radiation therapy growth, providing a balance between the short- and long-term effects of radiation therapy. The M_d, M_p, and M_{dp} models are then fit to the measured 3-dimensional tumor cell count time courses. The estimated model parameters are then used to predict future tumor growth and response. The discrepancy between the model prediction and the measured data is assessed at the post−radiation therapy time points. The model prediction is also compared with postmortem histologic analysis.

Methods and Materials

In vivo experiments

The experimental procedures were approved by our Institutional Animal Care and Use Committee. Rats were anesthetized with 2% isoflurane in 98% oxygen for all imaging, surgical, and irradiation procedures. Twelve female Wistar rats (257 ± 9 g, mean ± 95% confidence interval) were anesthetized and inoculated intracranially with 10^5 C6 glioma cells via stereotaxic injection on day 0. On day 8, permanent jugular catheters were placed in each rat for injection of an MRI contrast agent. Rats were imaged 3 times before treatment (days 10, 12, and 14, or t_1 through t_3) and 4 times after treatment (days 16.5, 18.5, 20.5, and 22.5, or t_4 through t_7). Magnetic resonance images were acquired using a 9.4T horizontal-bore magnet (Agilent, Santa Clara, CA). A pulsed

gradient fast spin echo DW-MRI (24, 25) sequence was used to measure the apparent diffusion coefficient (ADC), which was then used to estimate tissue cellularity as previously described (8, 9, 26-28). A T_1 map acquired using an inversion-recovery snapshot experiment was used to identify anatomic regions. A spoiled gradient echo CE-MRI experiment was used to identify tumor regions of interests after the injection of a 200-μL bolus (0.05 mmol kg^{-1}) of gadolinium-diethylenetriamine-pentaacetic acid (Gado-DTPA; BioPal, Worcester, MA). Magnetic resonance images were acquired over a 32 × 32 × 16-mm^3 field of view sampled with a 128 × 128 × 16 matrix (250 × 250 × 1000-μm voxel resolution). Additional MRI experimental details are reported in the Supplementary Material (available online at www.redjournal.org).

Rats were irradiated with 20 Gy (n = 5) or 40 Gy (n = 7) at a dose rate of 2.3 Gy/min with a Therapax DXT 300 x-ray machine (300 kVp/10 mA; Pantak, East Haven, CT) on day 14.5 (t_{rt}). Large single-fraction doses were selected for this initial study to elicit distinct responses for model development and validation. During the irradiation protocol, rats were shielded to minimize exposure outside of the brain. At the conclusion of the last imaging study, animals were killed, and the brain tissue was prepared for histologic sectioning and staining with hematoxylin and eosin and Ki-67. Additional histology details are reported in the Supplementary Material (available online at www.redjournal.org).

Biophysical models of tumor growth

Tumor growth is modeled using Equation 1, which describes the change in the distribution and number of tumor cells due to the random movement of tumor cells (first term on the right-hand side), the proliferation of cells (second term on the right-hand side), and the death of cells due to radiation therapy (third term on right-hand side):

$$\frac{\partial N(\bar{x},t)}{\partial t} = \nabla\cdot\left[\theta_{max}D(\bar{x},t)\nabla\left(\frac{N(\bar{x},t)}{\theta(\bar{x})}\right)\right] + k_p(\bar{x})\cdot RT_p(\bar{x},t)\cdot N(\bar{x},t)\left(1-\frac{N(\bar{x},t)}{\theta(\bar{x})}\right) - RT_d(\bar{x},t)\cdot N(\bar{x},t) \quad (1)$$

where the number of tumor cells at 3-dimensional position $\bar{x}$ and time t is $N(\bar{x},t)$, θ_{max} is the maximum number of cells that can physically fit in a voxel (50,970 cells), $D(\bar{x},t)$ is a mechanically coupled tumor cell diffusion coefficient (8, 9, 29, 30) (details in the Supplementary Material; available online at www.redjournal.org), $\theta(\bar{x})$ is the local carrying capacity, $k_p(\bar{x})$ is the local proliferation rate, $RT_p(\bar{x},t)$ is a post−radiation therapy proliferation function, and $RT_d(\bar{x},t)$ is a post−radiation therapy death function. $RT_p(\bar{x},t)$ is represented by a piecewise function, as in Equation 2:

$$RT_p(\bar{x},t) = \begin{cases} f_{p,rt}(\bar{x}) & t \geq t_{rt} \\ 1 & t < t_{rt} \end{cases} \quad (2)$$

where $f_{p,rt}$ is a reduced proliferation fraction. In this implementation we are assuming that the long-term effects of radiation will simply reduce the number of proliferating cells or the effective proliferation rate. Thus, this model does not consider long-term cell death or delayed cell death. Similarly, $RT_d(\bar{x},t)$ is also represented by a piecewise function, as in Equation 3:

$$RT_d(\bar{x},t) = \begin{cases} k_{d,rt}(\bar{x}) & t = t_{rt} \\ 0 & t \neq t_{rt} \end{cases} \quad (3)$$

where $k_{d,rt}$ is the post−radiation therapy death rate. The cell death term is assumed to occur instantaneously over a single time step. We note that although the LQ model is not explicitly used, the M_d model plays an equivalent role. Specifically, the model parameter $k_{d,rt}$ could be replaced with an LQ formulation of cell survival (as done in reference [17]). Instead of fitting for a spatially varying $k_{d,rt}$, we could fit for a spatially varying α (and assume a fixed α/β ratio and uniform dose distribution). The end result would still be a fraction of cells that do not survive radiation therapy. We decided to then simplify the model to capture this effect as a single parameter that implicitly takes into account dose and radiosensitivity. These 3 models represent natural extensions of the LQ model to incorporate the instantaneous and delayed effects of radiation therapy and do so using imaging data that are available in the clinical setting.

Measured values of $N(\bar{x},t)$, $N_{meas}(\bar{x},t)$, are obtained using DW-MRI before and after radiation therapy (27, 28, 30). Pretreatment (t_1 through t_3) measurements of $N(\bar{x},t)$ are used to solve an inverse problem (28, 30) to return estimates of $\theta(\bar{x})$, $k_p(\bar{x})$, and tumor cell diffusion. Similarly, posttreatment measurements (t_4 through t_5) are then used to solve an inverse problem to estimate $k_{d,rt}$ and $f_{p,rt}$ voxel-wise within the tumor. Model parameters were calibrated using a Levenberg-Marquardt least squares algorithm (31, 32), which minimizes the error between the modeled and measured cellularity. For the M_d model, $k_{d,rt}$ is estimated, and $f_{p,rt}$ is set to 1. For the M_p model, $f_{p,rt}$ is estimated, and $k_{d,rt}$ is assigned to 0. For the M_{dp} model, both $k_{d,rt}$ and $f_{p,rt}$ are estimated. Literature values used for mechanical tissue properties (discussed in the Supplementary Material; available online at www.redjournal.org) were assigned from excised rat brain samples (33, 34), though it would be preferable to measure these parameters on an individual basis (potentially through MR elastography [35]). Literature values were also used to assign cell packing density (36) and the average cell size (37). We further assume that the packing density and cell size remain constant throughout the duration of the experiment. (Future efforts could use advanced diffusion approaches to measure, for example, changes in cell size [38, 39]). The estimated model parameters are then used in a forward evaluation of the model system, $N_{model}(\bar{x},t)$, to predict tumor growth at t_6 and t_7. The finite difference method was used to solve

Equation 1 using a 3 dimension in space (250 × 250 × 1000-μm grid spacing) and fully explicit in time simulation (time step of 0.01 days). (The Supplementary Materials [available online at www.redjournal.org] expand on the in vivo and computational details.)

Error analysis

The model prediction error was assessed using 2 metrics on days t_6 and t_7. First, the differences between the predicted and measured tumor size and shape were assessed by calculating the percent error in tumor volume and the average surface distance (ASD), respectively. Second, within overlapping regions of the predicted and measured tumors, the percent error in cell number was calculated. The percent error in tumor volume was determined by calculating the percent difference between the predicted and the measured estimates of tumor volume. The ASD reports the average minimum distance between a voxel on the surface of the model tumor volume and a voxel on the surface of the measured tumor volume. The error in model fit post–radiation therapy was calculated using a weighted sum squared error (wSSE), described in the Supplementary

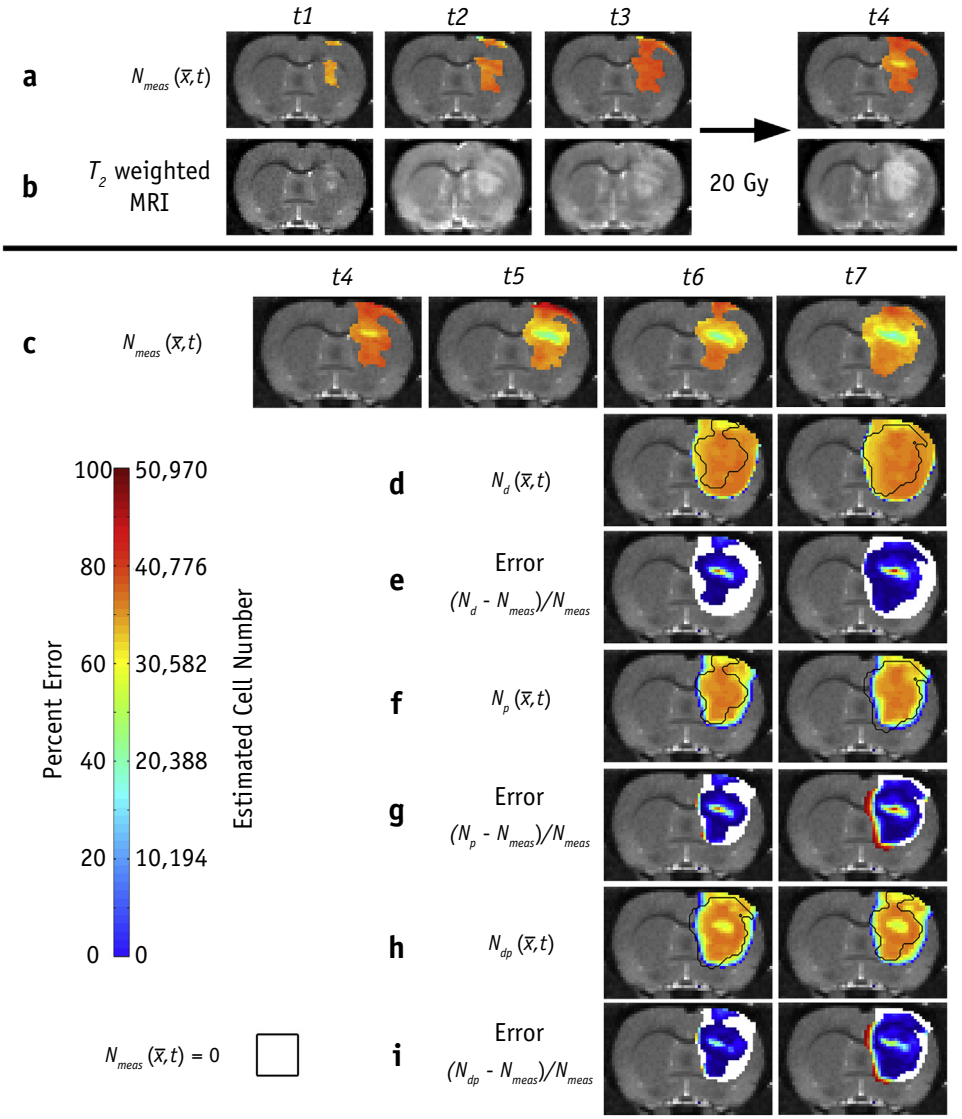

Fig. 1. Measured and simulated $N(\bar{x}, t)$ for a rat irradiated with 20 Gy. The measured (rows a-c) and simulated (rows d, f, and h) $N(\bar{x}, t)$ are shown for a rat irradiated with 20 Gy. The black lines in rows d, f, and h represent the boundaries of $N_{meas}(\bar{x}, t)$. Percent error between the measured and simulated $N(\bar{x}, t)$ are also shown in rows e, g, and i, with the white space indicating areas where $N_{meas}(\bar{x}, t) = 0$. The tumor size was overestimated for the M_d and M_{dp} models at t_6 and t_7 compared with the M_p model. The M_p and M_d models had greater than 60% error (rows e, g, and i) in low cell density areas observed in $N_{meas}(\bar{x}, t)$ (row c). The pretreatment parameters D_0 and mean k_p were 1.19 $\mu m^2/d$ and 2.16 d^{-1}, respectively. The mean posttreatment parameters were as follows: $f_{p,Mp} = 0.38 \pm 0.06$; $f_{p,Mdp} = 0.36 \pm 0.01$; $k_{d,Md} = 0.47 \pm 0.06$; and $k_{d,Mdp} = 0.34 \pm 0.02$.

Materials (available online at www.redjournal.org), to equally weight each time point according to the total number of cells at each time point. At the voxel level, the percent difference in cell number was calculated between the model and measurement wherever $N_{meas}(\bar{x},t)$ was greater than 0. All results are reported as the mean and 95% confidence interval when appropriate. A 1-way analysis of variance was used to evaluate the differences in global and local errors between the model fits within treatment groups. Tukey's honest significant difference test was then used for pair-wise comparisons. A P value of $<.05$ was considered significant. Pearson's correlation coefficient (r) was calculated between the histology measurements and model parameters.

Results

Figures 1 and 2 show measured and modeled number of tumor cells, as well as the percent difference between the 2, from the central tumor slice for representative rats from the 20-Gy and the 40-Gy groups, respectively. For the rat irradiated with 20 Gy, the predictions of the M_d model (row d) overestimate tumor size (error greater than 55.7%) on t_6 and t_7 compared with the M_p and M_{dp} models (error less than 17.0% and 9.6%, respectively). No significant differences were observed between the models at the voxel level (mean error ranged from 10.2% to 13.2%). Importantly, the M_d and M_p models fail to capture the developing low cell

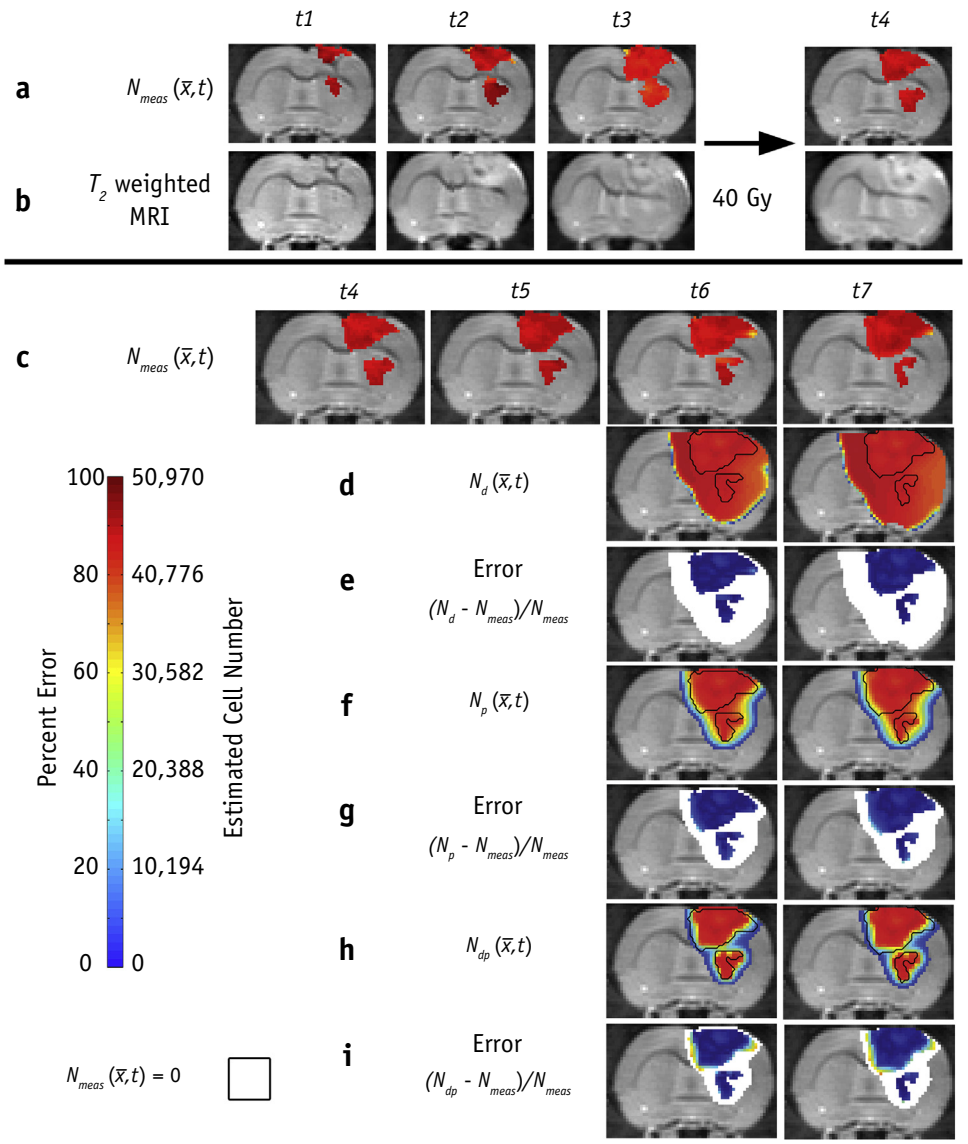

Fig. 2. Measured and simulated $N(\bar{x},t)$ for a rat irradiated with 40 Gy (The data are presented in an identical fashion to Fig. 1). The M_d model overestimated tumor size on days t_6 through t_7 (row d). The M_p and M_{dp} models more closely matched the tumor shape and size at all time points (rows f and h). The pretreatment parameters D_0 and mean k_p were 2.01 $\mu m^2/d$ and 4.23 day^{-1}, respectively. The mean posttreatment parameters were as follows: $f_{p,Mp} = 0.06 \pm 0.01$; $f_{p,Mdp} = 0.25 \pm 0.01$; $k_{d,Md} = 0.72 \pm 0.04$; and $k_{d,Mdp} = 0.63 \pm 0.03$.

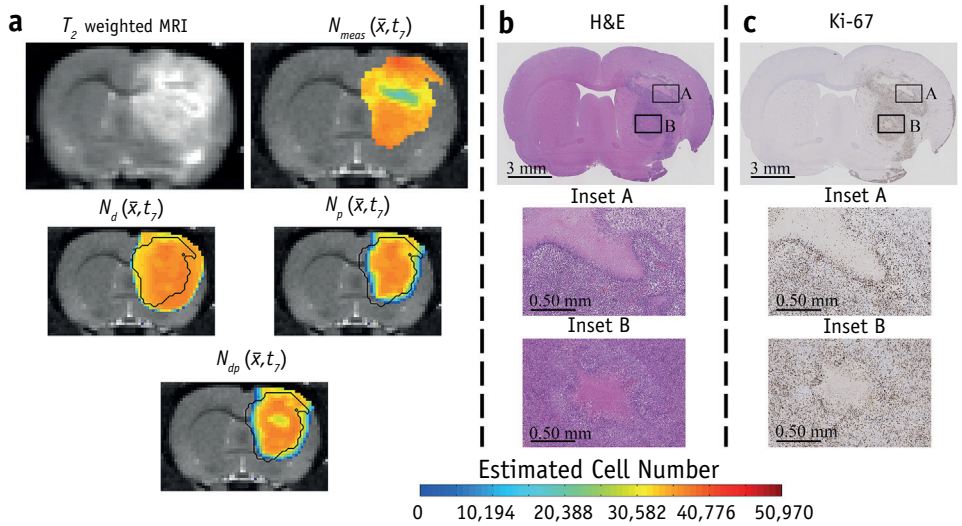

Fig. 3. Model and measured $N(\bar{x},t)$ compared with histology for a rat irradiated with 20 Gy. Magnetic resonance imaging measured and simulated $N(\bar{x},t)$ (panel a) are compared with equivalent hematoxylin and eosin (H&E) (panel b) and Ki-67 (panel c) stained sections for a rat irradiated with 20 Gy. Insets A and B indicate areas of low cell density and low positive Ki-67 stained cells. In panel c, positive staining (brown) was seen throughout the tumor, with the exception of the low cell density regions (insets A and B). The low cell density regions in $N_{meas}(\bar{x},t_7)$ are present in inset A from the hematoxylin and eosin slide. (A color version of this figure is available at www.redjournal.org.)

density region on days t_6 through t_7 (row c, resulting in greater than 50% error in these regions [rows e, g, i]), whereas the M_{dp} model exhibits lower error (less than 30%) in these regions.

For the rat irradiated with 40 Gy, the predictions of the M_d model had high error in tumor volume (greater than 114.9%), whereas the M_p and M_{dp} had lower error in tumor volume (less than 23.5% and 10.5%, respectively). At the voxel level, no significant difference was observed among the 3 models (average error less than 5.1%).

Figures 3 and 4 compare the central imaging slice with histologic sections from the same representative rats in Figures 1 and 2. For the rat irradiated with 20 Gy, low cell density regions (2281 $\pm$ 238 cells/mm^2) in $N_{meas}(\bar{x},t_7)$, panel a, are also present in the hematoxylin and eosin slice (panel b, inset A), whereas a second low density region (panel b, inset B) is not visible in this imaging slice. A high level of positive stained Ki-67 cells (73.95% $\pm$ 4.56%) is observed throughout the tumor region. For the rat irradiated with 40 Gy, an average cell density of 6336 $\pm$ 334 cells/mm^2

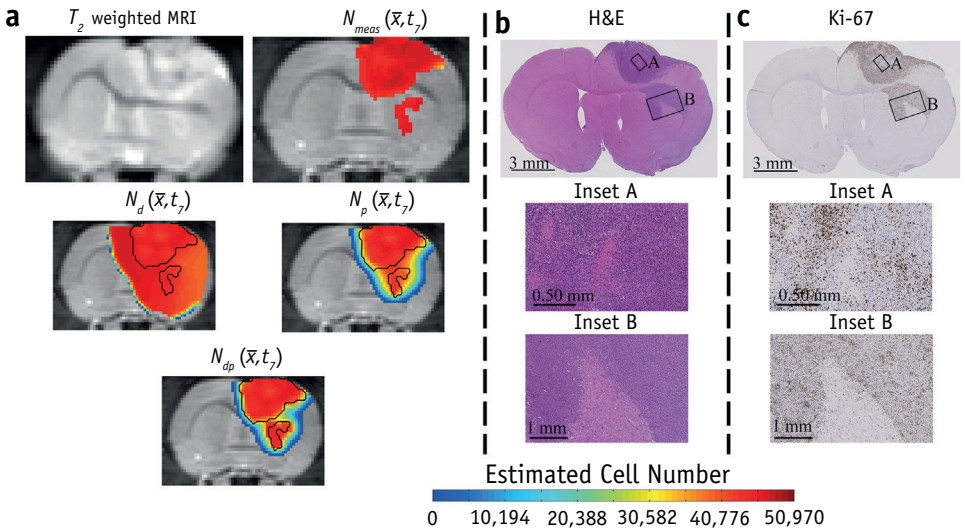

Fig. 4. Model and measured $N(\bar{x},t)$ compared with histology for a rat irradiated with 40 Gy (The data are presented in an identical fashion to Fig. 3). Very few areas of low cell density (column b, inset A) were observed throughout the tumor. Column c shows a Ki-67−stained tissue section in which clusters of proliferating cells were observed throughout the tumor. *Abbreviation:* H&E = hematoxylin and eosin.

was observed in the tissue sections. High cell density is observed in both insets A and B, although there are a few low cell density regions (inset A) that appear throughout the tumor. Fewer positive Ki-67 stained cells (64.53% ± 2.90%) were observed compared with the rat irradiated with 20 Gy. The necrosis observed in the rat irradiated with 20 Gy, but not the one irradiated with 40 Gy, is likely due to inter-animal variability in tumor growth and response.

Figure 5 summarizes the error analysis for both groups of irradiated with 20 (panels a-c, g) and 40 Gy (panels d-f, h). A statistically significant ($P < .03$) reduction in error was observed at all time points for the M_p (error in tumor volume, ASD, error in voxel cell number) and M_{dp} (error in tumor volume, ASD) models compared with the M_d model. Similarly, for the rats irradiated with 40 Gy, a statistically significant ($P < .04$) reduction in error was observed at all time points for the M_p and M_{dp} (error in tumor volume, ASD, error in voxel cell number) models compared with the M_d model. For both treatment groups, significantly increased wSSE ($P < .05$) was observed for the M_p and M_d models compared with the M_{dp}. Additionally, the M_p model for the rats irradiated with 20 Gy had significantly decreased wSSE ($P < .01$) compared with the M_d model.

Table 1 reports the mean estimated model parameters and their correlation to the percent positive stained Ki-67 cells within tumor regions for both treatment groups. Significant differences were observed between doses for M_p and M_{dp} model parameters. Significant ($P < .05$) and strong correlation was observed for $f_{p,rt}$ for the rats irradiated with 40 Gy ($r = 0.99$) and $k_{d,rt}$ for the rats irradiated with 20 Gy ($r = -0.98$) parameters estimated for the M_{dp} model and Ki-67 staining.

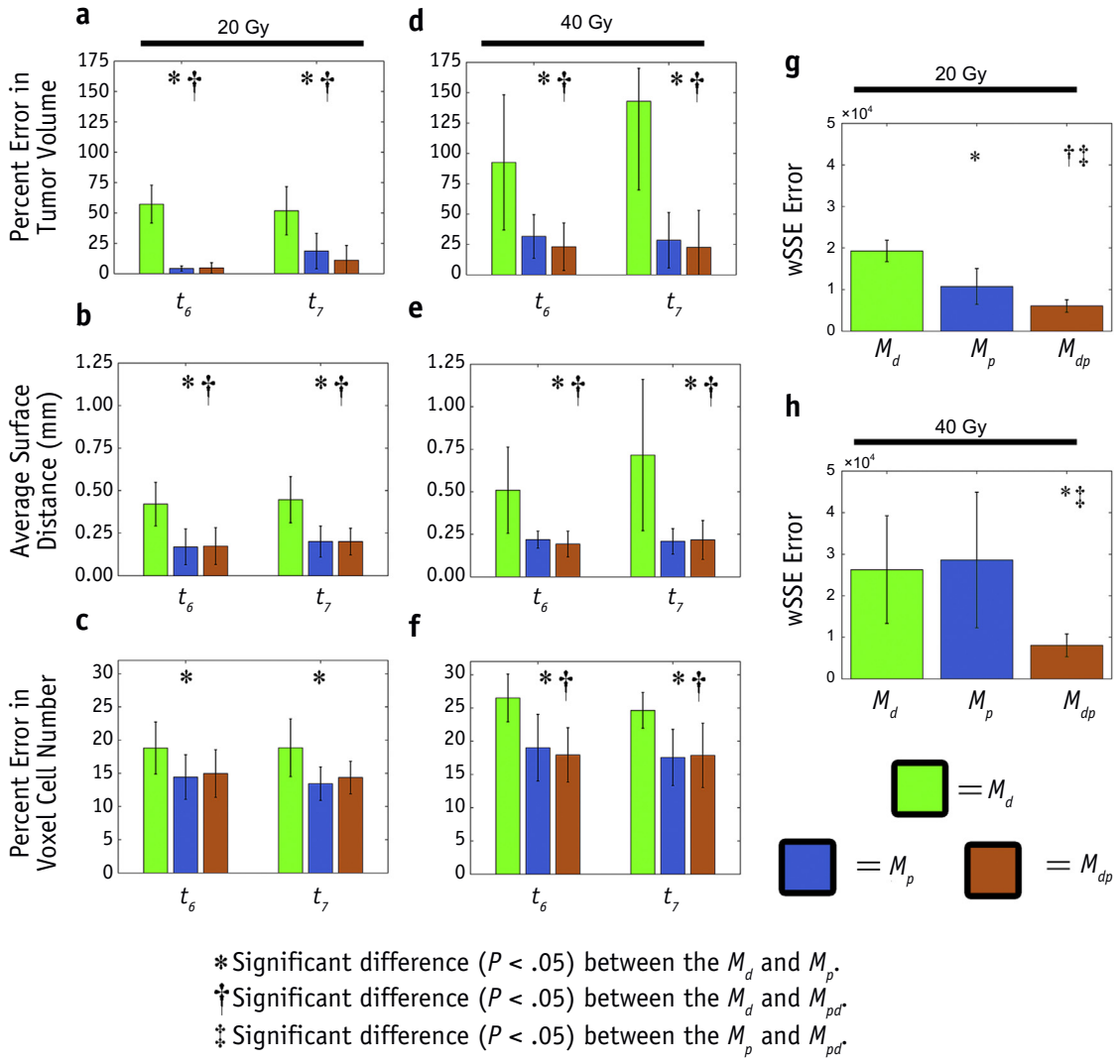

Fig. 5. Global and local error results for the 20-Gy (panels a-c) and 40-Gy (panels d-f) groups are reported as the mean and 95% confidence interval from day t_4 through t_7. The weighted sum squared error (wSSE) is also reported in panels g and h for the 20-Gy and 40-Gy rats, respectively. Generally, high global-level errors were observed for the M_d model for both treatment groups, whereas the M_{dp} model resulted in low global-level errors. All models resulted in low local-level errors for the 20-Gy group (panel c), whereas the M_d and M_{dp} models had lower error for the 40-Gy group (panel f).

Table 1 Estimated model parameters and correlation to histology

Model	Parameter	Estimated value, mean ± 95% CI	Model parameter vs percent positive stained Ki-67 cells	
			r	P
20 Gy				
M_d	$k_{d,rt}$	0.66 ± 0.24	−0.77	.23
M_p	$f_{p,rt}$	0.52 ± 0.27*	0.84	.16
M_{dp}	$k_{d,rt}$	0.31 ± 0.10*	−0.98	.02
	$f_{p,rt}$	0.30 ± 0.09*	0.90	.10
40 Gy				
M_d	$k_{d,rt}$	0.74 ± 0.12	−0.73	.25
M_p	$f_{p,rt}$	0.12 ± 0.07*	0.73	.27
M_{dp}	$k_{d,rt}$	0.61 ± 0.02*	−0.80	.20
	$f_{p,rt}$	0.22 ± 0.09*	0.99	.01

Abbreviation: CI = confidence interval.
* Statistically significant differences ($P < .05$) between treatment groups.

Discussion

The M_d model is a variation of the LQ model that has been previously applied (16, 40-42) to clinical data sets after fractionated radiation therapy. The M_d model reflects some of the short-term effects of radiation therapy, including cell death and shrinking of the tumor. Rather than assigning the death rate as the fraction of cells that die because of radiation therapy (16, 17), we fit the models to time course data to estimate a spatially varying death rate. The negative (although not statistically significant) correlation between $k_{d,rt}$ and percent positive stained Ki-67 cells suggests $k_{d,rt}$ may reflect observed tumor biology. The varied response between the 20-Gy and 40-Gy groups suggests that the M_d model may be more valid at low doses, where post−radiation therapy growth kinetics more closely match the untreated growth kinetics (Fig. E1; available online at www.redjournal.org).

The M_p model is another variation of the LQ model, in which the loss of proliferative ability is modeled as a decrease in the net proliferation rate compared with the pretreatment proliferation rate. Generally, the M_p model provided better model predictions compared with the M_d model. On the basis of the reduced doubling time observed after radiation therapy (Fig. E1; available online at www.redjournal.org), it was hypothesized that this model may be able to better describe the post−radiation therapy growth kinetics. The positive (although not statistically significant) correlation between $f_{p,rt}$ and percent positive stained Ki-67 cells, as well as the dose dependency of the mean $f_{p,rt}$, suggests $f_{dp,rt}$ may reflect the observed decrease in tumor proliferation. However, the M_p model results in high error in cases in which the tumor volume shrinks or indicates no growth after radiation therapy. The M_p model may more accurately describe growth at lower doses; however, it fails to capture decreases in tumor volume after therapy or areas of necrosis.

The M_{dp} model combines both short-term and long-term effects (22, 43). Both the M_p and M_{dp} resulted in decreased error (ie, in tumor volume, ASD, and voxel cell number) in model predictions, but the M_{dp} model may provide a better overall description owing to the decrease in wSSE compared with the M_p model. The statistically significant differences between the M_{dp} and M_p models for the wSSE metric, but not the other metrics, are likely to due to reduced error in both the calibration and prediction phases for the M_{dp} model, which only the wSSE metric assesses. The M_{dp} model may also provide improved predictions of intra-tumor heterogeneity (Figs. 1 and 3). Model parameters ($f_{p,rt}$ and $k_{d,rt}$) seemed to be dose specific, suggesting that a more explicit relationship between dose and $f_{p,rt}$ and $k_{d,rt}$ may exist; this is the subject of ongoing efforts. Comparison of model parameters with histologic staining indicated an inverse relationship between $k_{d,rt}$ and the percent positive stained Ki-67 cells and a positive relationship between $f_{p,rt}$ and Ki-67 staining. The histologic correlation for both parameters suggests that they may provide insight into the underlying tumor biology after radiation therapy (ie, delayed or altered proliferation, reduced number of proliferating cells). The M_{dp} model is a natural extension of previous modeling efforts (16, 17) of response to radiation therapy. The main benefit of the M_{dp} model is the incorporation of both single time-point cell kill and a long-term effect, which more accurately recapitulates in vivo observations of the persistent effect of radiation therapy.

There are several limitations to the present study. One limitation is in the interpretation of imaging measurements after radiation. In this work we use ADC measurements to estimate cell number. Several preclinical and clinical studies have demonstrated a strong correlation between histologic estimates of cellularity in human brain tumors (44), breast cancer (45), extracranial lesions (46), small animal models of breast cancer (47), and in vitro studies (26). There are, however, other factors (cell membrane

permeability [48], cell size, tortuosity [49], edema [50], necrosis [50]) that can also affect the measured ADC before and after treatment. This approach to transform ADC to cell number must, therefore, be regarded as a first-order approximation to the true tumor cellularity. Contrast-enhanced MRI enhancement may also potentially indicate false volume increases or decreases after radiation therapy (51). Pseudoprogression is often a result of increased inflammation, edema, and vessel permeability and can be challenging to distinguish from actual progression, and separating these 2 phenomena is an active area of research (52-55).

A second limitation is that there is a lack of histology for untreated rats to which the treated groups can be compared, as well as a lack of histology at the time of treatment. However, the dose-dependent decreases in Ki-67 have been observed by others (43).

A third limitation is the use of single large doses over the whole brain. Radiation therapy is more commonly delivered in small doses over several fractions with a more focal dose. Large single-fraction doses were selected for this initial study to provide 2 distinct treatment responses from which to test and validate the mathematical models. Ongoing studies will investigate smaller, fractionated dose response.

A fourth limitation is the lack of a validation of the pretreatment parameters. An additional imaging time point could be used to verify the pretreatment parameters; however, that will limit the number of posttreatment time points we could acquire. When applied to a cohort of untreated rats, this modeling approach resulted in less than 2.20% error in tumor volume, average surface distance less than 0.38 mm, and average percent error in voxel cell number less than 13.25% (30). On the basis of those results we have confidence in the ability of this framework to capture untreated tumor growth. Finally, in a data-limited setting (eg, standard-of-care clinical studies) this approach may not be tenable. However, with the advent of MRI-guided external beam radiation treatment (56), functional or anatomic data could be acquired on a per-fraction basis. This scenario would produce measurements that can be used to calibrate model parameters (and correct parameters as more data become available) that can be used to adapt the remaining treatment plans (57).

Conclusion

The models developed and analyzed within this study are an encouraging step toward the development of mathematically rigorous, individualized radiation therapy plans. After receiving 20 Gy, growth can be accurately described using the M_p or M_{dp} model. At higher doses the M_p and M_{dp} models both resulted in lower error in tumor volume, ASD, and voxel cell number, whereas the M_d model poorly described tumor response at high doses. Overall, the M_{dp} model provides a more complete characterization of the post–radiation therapy growth kinetics, although further model development is needed to more accurately characterize the heterogeneous response to radiation therapy within the tumor.

References

1. Barani IJ, Larson DA. Radiation Therapy of Glioblastoma. In: Raizer J, Parsa A, eds. *Current Understanding and Treatment of Gliomas. Cancer Treatment and Research*, vol 163. Cha: Springer; 2015.
2. Omuro A, DeAngelis LM. Glioblastoma and other malignant gliomas: A clinical review. *JAMA* 2013;310:1842-1850.
3. Yankeelov TE, Atuegwu N, Hormuth DA, Weis JA, Barnes SL, Miga MI, et al. Clinically Relevant Modeling of Tumor Growth and Treatment Response. *Sci Transl Med* 2013;5:187ps9.
4. Baldock A, Rockne R, Boone A, et al. From patient-specific mathematical neuro-oncology to precision medicine. *Front Oncol* 2013; 3:62.
5. Hogea C, Davatzikos C, Biros G. An image-driven parameter estimation problem for a reaction-diffusion glioma growth model with mass effects. *J Math Biol* 2008;56:793-825.
6. Konukoglu E, Clatz O, Menze BH, et al. Image guided personalization of reaction-diffusion type tumor growth models using modified anisotropic eikonal equations. *IEEE Trans Med Imaging* 2010; 29:77-95.
7. Clatz O, Sermesant M, Bondiau PY, et al. Realistic simulation of the 3-D growth of brain tumors in MR images coupling diffusion with biomechanical deformation. *IEEE Trans Med Imaging* 2005;24: 1334-1346.
8. Weis JA, Miga MI, Arlinghaus LR, Li X, Chakravarthy AB, Abramson V, et al. A mechanically coupled reaction-diffusion model for predicting the response of breast tumors to neoadjuvant chemotherapy. *Phys Med Biol* 2013;58:5851-5866.
9. Weis JA, Miga MI, Arlinghaus LR, Li X, Abramson V, Chakravarthy AB, et al. Predicting the Response of Breast Cancer to Neoadjuvant Therapy Using a Mechanically Coupled Reaction-Diffusion Model. *Cancer Res* 2015;75:4697-4707.
10. Atuegwu NC, Arlinghaus LR, Li X, Chakravarthy AB, Abramson VG, Sanders ME, et al. Parameterizing the Logistic Model of Tumor Growth by DW-MRI and DCE-MRI Data to Predict Treatment Response and Changes in Breast Cancer Cellularity during Neoadjuvant Chemotherapy. *Transl Oncol* 2013; 6:256-264.
11. Atuegwu NC, Gore JC, Yankeelov TE. The integration of quantitative multi-modality imaging data into mathematical models of tumors. *Phys Med Biol* 2010;55:2429-2449.
12. Liu Y, Sadowski SM, Weisbrod AB, et al. Patient specific tumor growth prediction using multimodal images. *Med Image Anal* 2014; 18:555-566.
13. Bondiau PY, Konukoglu E, Clatz O, et al. Biocomputing: Numerical simulation of glioblastoma growth and comparison with conventional irradiation margins. *Phys Med* 2011;27:103-108.
14. Weis JA, Miga MI, Yankeelov TE. Three-dimensional image-based mechanical modeling for predicting the response of breast cancer to neoadjuvant therapy. *Comput Methods Appl Mech Eng* 2017;314: 494-512.
15. Rana N, Weis JA, Miga MI, Thompson RC, Weaver KD, Chambless LB, et al. Image-Based Mathematical Modeling to Differentiate Radiation-Induced Necrosis From Tumor Recurrence Following Stereotactic Radiosurgery for Intracranial Metastasis. *Int J Radiat Oncol Biol Phys* 2017;96:E703.
16. Rockne R, Alvord EC, Rockhill JK, et al. A mathematical model for brain tumor response to radiation therapy. *J Math Biol* 2009;58: 561-578.

17. Rockne R, Rockhill JK, Mrugala M, et al. Predicting the efficacy of radiotherapy in individual glioblastoma patients in vivo: A mathematical modeling approach. *Phys Med Biol* 2010;55:3271-3285.
18. Corwin D, Holdsworth C, Rockne RC, et al. Toward patient-specific, biologically optimized radiation therapy plans for the treatment of glioblastoma. *PLoS One* 2013;8:e79115.
19. Holdsworth C, Corwin D, Stewart R, et al. Adaptive IMRT using a multiobjective evolutionary algorithm integrated with a diffusion-invasion model of glioblastoma. *Phys Med Biol* 2012;57:8271.
20. Badoual M, Gerin C, Deroulers C, et al. Oedema-based model for diffuse low-grade gliomas: Application to clinical cases under radiotherapy. *Cell Prolif* 2014;47:369-380.
21. Antipas VP, Stamatakos GS, Uzunoglu NK. A patient-specific in vivo tumor and normal tissue model for prediction of the response to radiotherapy. *Methods Inf Med* 2007;46:367-375.
22. Parthymou A, Kardamakis D, Pavlopoulos I, et al. Irradiated C6 glioma cells induce angiogenesis in vivo and activate endothelial cells in vitro. *Int J Cancer* 2004;110:807-814.
23. Bencokova Z, Pauron L, Devic C, et al. Molecular and cellular response of the most extensively used rodent glioma models to radiation and/or cisplatin. *J Neurooncol* 2008;86:13-21.
24. Maier SE, Sun Y, Mulkern RV. Diffusion imaging of brain tumors. *NMR Biomed* 2010;23:849-864.
25. Koh DM, Collins DJ. Diffusion-weighted MRI in the body: Applications and challenges in oncology. *Am J Roentgenol* 2007;188:1622-1635.
26. Anderson AW, Xie J, Pizzonia J, et al. Effects of cell volume fraction changes on apparent diffusion in human cells. *Magn Reson Imaging* 2000;18:689-695.
27. Atuegwu NC, Colvin DC, Loveless ME, Xu L, Gore JC, Yankeelov TE. Incorporation of diffusion-weighted magnetic resonance imaging data into a simple mathematical model of tumor growth. *Phys Med Biol* 2012;57:225-240.
28. Hormuth II DA, Weis JA, Barnes SL, Miga MI, Rericha EC, Quaranta V, et al. Predicting in vivo glioma growth with the reaction diffusion equation constrained by quantitative magnetic resonance imaging data. *Phys Biol* 2015;12:46006.
29. Garg I, Miga MI. Preliminary investigation of the inhibitory effects of mechanical stress in tumor growth. Proc SPIE. Proc. SPIE; 2008. bl 69182L−69182L−11.
30. Hormuth II DA, Weis JA, Barnes SL, Miga MI, Rericha EC, Quaranta V, et al. A mechanically-coupled reaction-diffusion model that incorporates intra-tumoral heterogeneity to predict in vivo glioma growth. *J R Soc Interface* 22 March 2017;14(128).
31. Marquardt DW. An algorithm for least-squares estimation of nonlinear parameters. *J Soc Ind Appl Math* 1963;11:431-441.
32. Levenberg K. A method for the solution of certain non-linear problems in least squares. *Q J Appl Math* 1944;2:164-168.
33. Elkin BS, Ilankovan AI, Morrison B III. A detailed viscoelastic characterization of the P17 and adult rat brain. *J Neurotrauma* 2011;28:2235-2244.
34. Lee SJ, King MA, Sun J, et al. Measurement of viscoelastic properties in multiple anatomical regions of acute rat brain tissue slices. *J Mech Behav Biomed Mater* 2014;29:213-224.
35. Huston J III. Magnetic resonance elastography of the brain. In: Venkatesh S, Ehman R, eds. Magnetic Resonance Elastography. New York: Springer; 2014. p. 89-98.
36. Martin I, Dozin B, Quarto R, et al. Computer-based technique for cell aggregation analysis and cell aggregation in in vitro chondrogenesis. *Cytometry* 1997;28:141-146.
37. Rouzaire-Dubois B, Milandri JB, Bostel S, et al. Control of cell proliferation by cell volume alterations in rat C6 glioma cells. *Pflugers Arch* 2000;440:881-888.
38. Panagiotaki E, Walker-Samuel S, Siow B, et al. Noninvasive quantification of solid tumor microstructure using VERDICT MRI. *Cancer Res* 2014;74:1902-1912.
39. Jiang X, Li H, Xie J, et al. In vivo imaging of cancer cell size and cellularity using temporal diffusion spectroscopy. *Magn Reson Med* 2017;78:156-164.
40. Prokopiou S, Moros EG, Poleszczuk J, et al. A proliferation saturation index to predict radiation response and personalize radiotherapy fractionation. *Radiat Oncol* 2015;10:1-8.
41. Jeong J, Shoghi K, Deasy J. Modelling the interplay between hypoxia and proliferation in radiotherapy tumour response. *Phys Med Biol* 2013;58:4897.
42. Titz B, Jeraj R, Jeraj BT, et al. An imaging-based tumour growth and treatment response model: Investigating the effect of tumour oxygenation on radiation therapy response. *Phys Med Biol* 2008;53:4471.
43. Bauman GS, Fisher BJ, McDonald W, et al. Effects of radiation on a three-dimensional model of malignant glioma invasion. *Int J Dev Neurosci* 1999;17:643-651.
44. Sugahara T, Korogi Y, Kochi M, et al. Usefulness of diffusion-weighted MRI with echo-planar technique in the evaluation of cellularity in gliomas. *J Magn Reson Imaging* 1999;9:53-60.
45. Guo Y, Cai YQ, Cai ZL, et al. Differentiation of clinically benign and malignant breast lesions using diffusion-weighted imaging. *J Magn Reson Imaging* 2002;16:172-178.
46. Humphries PD, Sebire NJ, Siegel MJ, et al. Tumors in pediatric patients at diffusion-weighted MR imaging: Apparent diffusion coefficient and tumor cellularity. *Radiology* 2007;245:848-854.
47. Barnes SL, Sorace AG, Loveless ME, Whisenant JG, Yankeelov TE. Correlation of tumor characteristics derived from DCE-MRI and DW-MRI with histology in murine models of breast cancer. *NMR Biomed.* 2015;28:1345-1356.
48. Latour LL, Svoboda K, Mitra PP, et al. Time-dependent diffusion of water in a biological model system. *Proc Natl Acad Sci U S A* 1994;91:1229-1233.
49. van der Toorn A, Syková E, Dijkhuizen RM, et al. Dynamic changes in water ADC, energy metabolism, extracellular space volume, and tortuosity in neonatal rat brain during global ischemia. *Magn Reson Med* 1996;36:52-60.
50. LaViolette PS, Mickevicius NJ, Cochran EJ, et al. Precise ex vivo histological validation of heightened cellularity and diffusion-restricted necrosis in regions of dark apparent diffusion coefficient in 7 cases of high-grade glioma. *Neuro Oncol* 2014;16:1599-1606.
51. Hygino da Cruz LC, Rodriguez I, Domingues RC, et al. Pseudoprogression and pseudoresponse: Imaging challenges in the assessment of posttreatment glioma. *AJNR Am J Neuroradiol* 2011;32:1978-1985.
52. Boxerman JL, Ellingson BM, Jeyapalan S, et al. Longitudinal DSC-MRI for distinguishing tumor recurrence from pseudoprogression in patients with a high-grade glioma. *Am J Clin Oncol* 2017;40:228-234.
53. Wang S, Martinez-Lage M, Sakai Y, et al. Differentiating tumor progression from pseudoprogression in patients with glioblastomas using diffusion tensor imaging and dynamic susceptibility contrast MRI. *AJNR Am J Neuroradiol* 2016;37:23-36.
54. Hu LS, Eschbacher JM, Heiserman JE, et al. Reevaluating the imaging definition of tumor progression: Perfusion MRI quantifies recurrent glioblastoma tumor fraction, pseudoprogression, and radiation necrosis to predict survival. *Neuro Oncol* 2012;14:919-930.
55. Young RJ, Gupta A, Shah AD, et al. Potential utility of conventional MRI signs in diagnosing pseudoprogression in glioblastoma. *Neurology* 2011;76:1918-1924.
56. Lagendijk JJW, Raaymakers BW, van Vulpen M. The magnetic resonance imaging-linac system. *Semin Radiat Oncol* 2014;24:207-209.
57. Kostelich EJ, Kuang Y, McDaniel JM, et al. Accurate state estimation from uncertain data and models: An application of data assimilation to mathematical models of human brain tumors. *Biol Direct* 2011;6:64.